Proceedings World Geothermal Congress 2020+1
Reykjavik, Iceland, April - October 2021

Experimental and Numerical Study of an Expandable Multi-layer Thermoelectric Generator System

Changwei LIU[1,2], Xiaoming TIAN[1], Kewen LI[1,2,] *, B.M. MAHLALELA[1], Yuhao ZHU[1], Jianbin ZHOU[3], Zhiming YAN[3]

[1] China University of Geosciences (Beijing), China

[2] Stanford University, CA, USA

[3]Yangquan Coal Industry (Group) Co., Ltd., Yangquan, China

*kewenli@stanford.edu

Keywords: Thermoelectric; Thin Plate Framework; Geothermal and Waste Heat Energy; Low Temperature; Modeling and Optimization

ABSTRACT

A thermoelectric generator (TEG) system can transfer the thermal energy to electric energy directly. However, most of the frameworks for holding TEG chips and for heat exchange are expensive. The high cost spent on the heat exchange and frameworks reduces competitiveness of the TEG systems and hinders the large-scale application of thermoelectric technology. In this paper, a TEG power generation system is designed by using a specific type of thin plate framework (TPF) in order to reduce the cost, obtain higher heat-to-electricity efficiency, and increase the power density. Experiments have been conducted to measure the power output at the conditions of different water flow rates and temperature differences between hot and cold sides. Comparisons with the heat exchange frameworks often used in conventional TEG systems have also been done. Numerical TEG models and the corresponding modeling methodology have been established for complex TEG systems with multi-layers of TPF. Modellings were then conducted and the modeling results are tested by the experimental data. The TEG with thin plate framework could be an option for low enthalpy geothermal resources and distributed waste heat.

1. INTRODUCTION

With the global concerns about environmental issues, researchers are considering the potential of geothermal energy to replace fossil fuels and meet the obligations of reducing the amount of carbon emission(Jacobson et al. 2015; Jacobson and Delucchi 2011). Geothermal power generation is reliable and independent from short term weather fluctuations compared with photovoltaic or wind turbine power generation. Electricity generated by geothermal energy has fewer fluctuations when accessed from the power grid. Temperature is a very important parameter in geothermal systems. Generally, there are three grades of the extractive working fluids: high temperature (> 180 ºC), intermediate temperature (100 to 180 ºC), and low temperature (30 to 100 ºC), respectively. The geothermal gradient may vary dramatically in different regions (Lund and Zoback 1999; Saemundsson 2013). Geothermal power generation either directly uses the steam extracted from geothermal reservoirs (for high temperature resources) or vaporizes relatively low boiling point organic fluids in a binary turbine (for low temperature resources).

As can be seen from Figure 1 (Li et al. 2015), the total capacity of geothermal power generation has been increasing over the years. However, geothermal power has been left behind wind and solar in terms of both growth rate and installed capacity. The main reasons may be high initial investment, long payback time and construction time, difficulty to assess resource and difficulty to modularize. It has been tested and shown that current commercially available geothermal technologies can only yield a linear, instead of an exponential, and a very slow growth rate in the last four decades. Li et al (Li et al. 2015) point out that TEG technology may be the possible solution to make breakthrough because it has almost all of advantages of PVs which is easy to modularize and has a short construction time. A TEG chip comprises of p-type and n-type semiconductor thermoelectric legs fastened between two hot/cold ceramic plates (Goldsmid and Nolas 2002). A voltage is induced due to the Seebeck effect when there is a temperature gradient across the legs. Generally, TEG technology can be applied in the field of recovering waste heat for generating electricity (Maneewan and Chindaruksa 2009; Demir and Dincer 2017; Huang et al. 2018), harvesting solar energy combined with photovoltaic technology (Bamroongkhan, Lertsatitthanakorn, and Soponronnarit 2019), etc. There have been studies about thermal losses (Lee et al. 2018), properties of thermoelectric materials (Kim, Liu, and Ren 2017), heat exchanger(Lv et al. 2018; Forooghi and Hooman 2014), etc. The effect of the TEG dimensions and flow characteristics on the conversion efficiency has been examined for a stack with counter-flow configuration (Yu and Zhao 2007; Suter, Jovanovic, and Steinfeld 2012; Wang et al. 2014; Liu, Chen, and Li 2014).

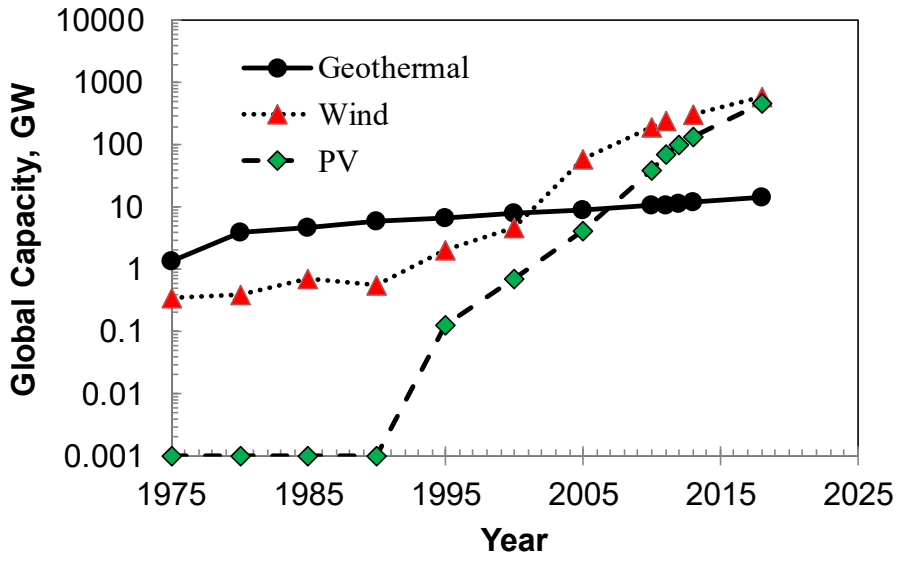

Figure 1: Comparison of installed global power capacity for individual energy types(Li et al. 2015).

However, there are two aspects which impede the application of thermoelectric generators in geothermal fields. One is the low efficiency of thermoelectric materials, and the other is the high cost of the thermoelectric power generation system, especially the heat exchanger parts. Most of the recently conducted studies are focused on the materials, and the achievements are promising. The system design lags a little behind (Tan, Zhao, and Kanatzidis 2016). The cost of the framework for holding TEG chips and for heat exchange is still very high, which reduces the competitiveness and hinders the large-scale application of thermoelectric technologies.

This study designed and applied a typical category of thin plate framework (TPF) -TEG stack that combines the thermoelectric generator (TEG) with TPFs. The power density of TPF-TEG is higher, and the cost per watt of TPF-TEG is 3-5 times cheaper than other existing models. The numerical model describing the TPF-TEG stack has been developed. The modeling results have been tested using the experimental data.

2. DESIGN OF THERMOELECTRIC STACKS

The thermoelectric stack configuration is shown in Figure 2. For this study, we used water as working fluid, which is cheap and easy to operate. The thermal energy is directly converted into electricity by using TEG chips when there is a temperature difference (see Figure 4 for TEG chip). Note that the material used to make TEG chips are bismuth tellurite (Bi_2Te_3). The original TPF is modified to make room for TEG arrays and provide hot/cold water channels. The upper and lower plates of the TEG array are directly in contact with the TEG chips and water. A bottom cold water channel layer, middle TEG chips array layer and upper hot water channel layer are combined into a TPF-TEG unit. Each TPF-TEG unit is separated by steel or other type of metal plates. One TEG array contains 18 TEG chips. The heat of hot water can be provided by hot fluids or geothermal resources. Hot water is pumped through the manifold into the hot water channel and operates with cold water channel in counter-flow configuration. All the TEG chips are connected in series as the power source and there is an external load in the circuit.

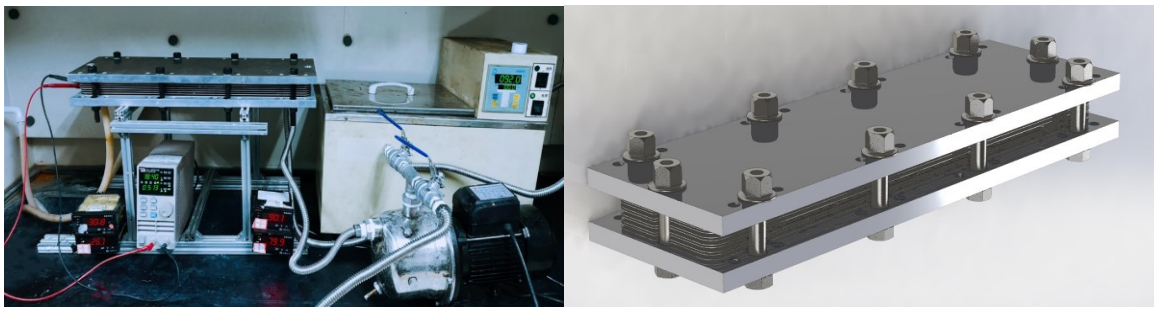

Figure 2: Experimental prototype of ten-unit TPF-TEG stack.

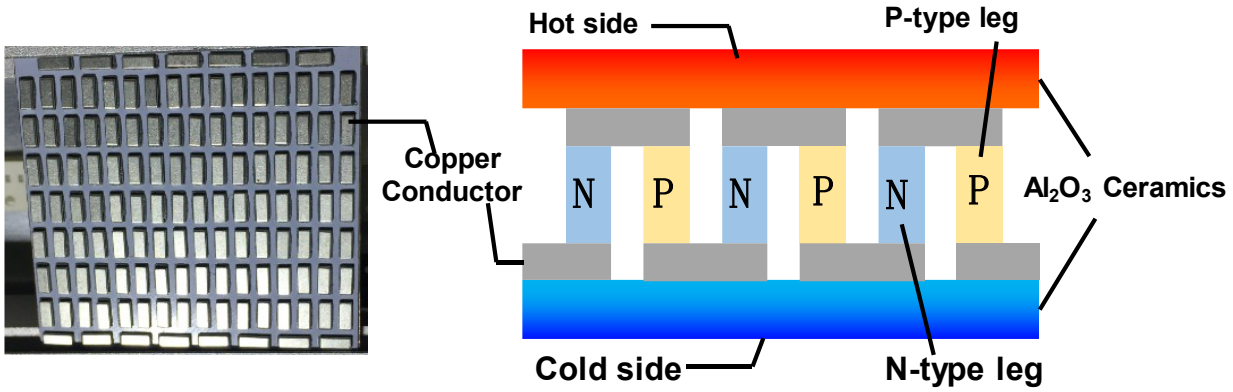

Figure 3: Top view (left) and cross-section view (right) of TEG chip.

As shown in Figure 2, the dimension of TPF is 550 mm×130 mm. The thickness of the steel plate of the TPF is 0.5 mm, which is used for separating TPF-TEG units. Both the upper and lower plate of TEG chips arrays are made of steel and have a thickness of 0.6 mm. Two water inlets and two water outlets are placed at the corner of the whole TPF-TEG stack, which are 31 mm and 240 mm to the center of the stack in width and length direction, respectively. Hot- and cold-water flow in the channels in-between the TPF plate and TEG plate in a counter-flow configuration. Water is delivered into the inlet on one side of the plate and flows to the surface of the plate, then out through the outlet on the other side of the plate. The hot water, which was supplied by the thermostatic water bath circulator, simulated the geothermal or hot water and provided heat for the generators. The cooling cycle was composed of a water pump and a water container. Thermal couples for temperature measurements (thermocouple grade wire, –270 to 1260 °C; extension wire, 0 to 200 °C; special limits of error: ±0.4%) and displayers were installed at the inlet and outlet pipes. The values of voltage, current and power can be collected by the electrical multi-meter (Test range: 0-150 W, 0-60 V, 1 mA-30 A; accuracy: ±1%+0.5% FS), as listed in Figure 4. More units can be enclosed into the system when conducting experiments. The length, width, and thickness of the TEG chip are 40 mm, 40 mm and 3 mm, respectively.

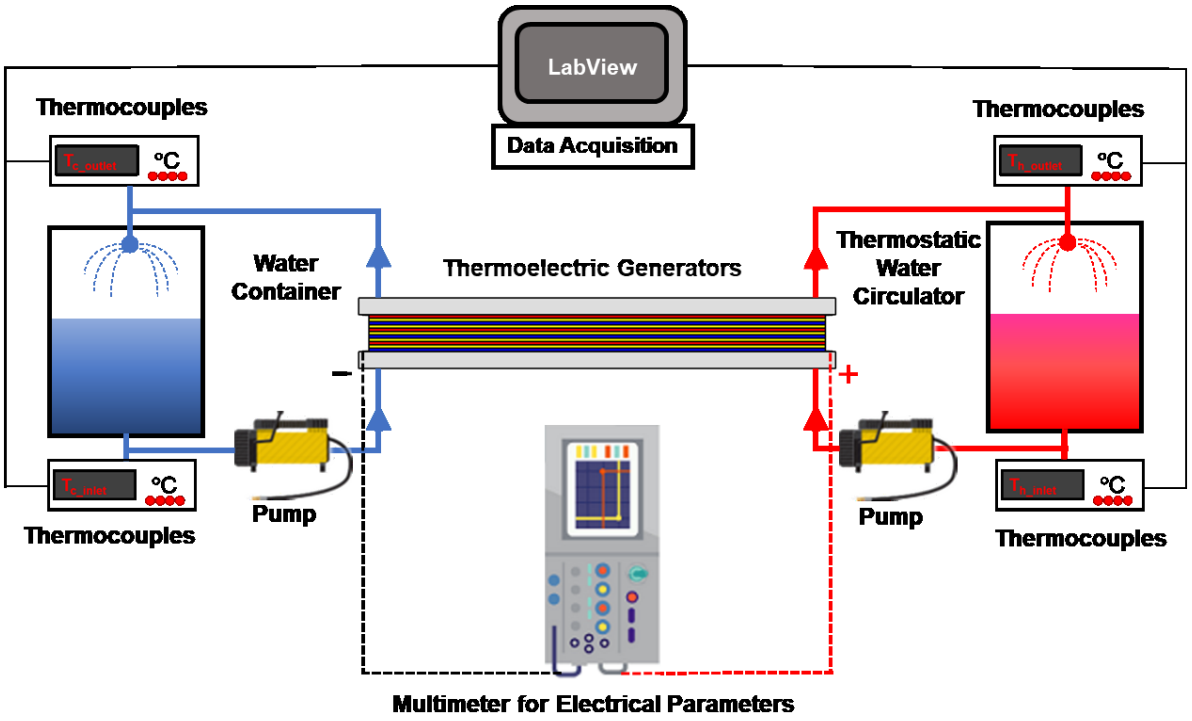

Figure 4: Schematic of the stack test.

3. EXPERIMENTAL DATA OF POWER GENERATED FROM THE TPF-TEG.

For this study, we performed three scenarios of experiments with different number of TPF-TEG units: one unit, five units, and ten units, respectively. Each scenario has specific parameters of the inlet temperature and volumetric flow rate of hot and cold water. The power output was measured when the external load was equal to the internal resistance, which means the power data are the maximum power output for each scenario. The outlet temperatures of hot and cold water were measured and recorded when the whole physical model was at the stationary condition. The experimental data are shown in Table and Figure 5. The experimental results of one unit apparatus will be used to compare with those reported in our previous study (Chen et al. 2017) and all of the results listed in Table 1 will be utilized to test our modeling data.

Table 1: The parameters and experimental data for three scenarios.

	Experimental data							
	T_{hot_in} (°C)	T_{cold_in} (°C)	Q_{hot} (L/min)	Q_{cold} (L/min)	△T (°C)	Power (W)	T_{hot_out} (°C)	T_{cold_out} (°C)
One unit	50	26.4	16.7	11.1	23.6	1.7	49.1	26.9
	60	26.4	16.7	11.1	33.6	3.4	58.5	27.2
	70	26.4	16.7	11.1	43.6	5.6	67.0	27.5
	80	26.4	12.2	11.1	53.6	8.3	75.3	27.9
	90	26.4	10.5	11.1	63.6	11.2	84.0	28.1
Five units	50	26.1	17.1	12.0	23.9	7.1	48.0	28.4
	60	26.1	17.1	12.0	33.9	14.3	57.2	29.0
	70	26.1	17.1	12.0	43.9	23.3	65.0	29.7
	80	26.1	12.5	12.0	53.9	34.8	73.5	30.3
	90	26.1	10.7	12.0	63.9	45.0	79.9	30.8
Ten units	50	26.0	16.7	9.1	24.0	11.2	46.8	29.3
	60	26.0	16.7	11.8	34.0	21.4	54.5	30.3
	70	26.0	15.0	11.8	44.0	36.9	62.9	31.7
	80	26.0	13.3	11.8	54.0	52.3	69.8	33.0
	90	26.0	11.1	11.8	64.0	70.2	75.6	34.0

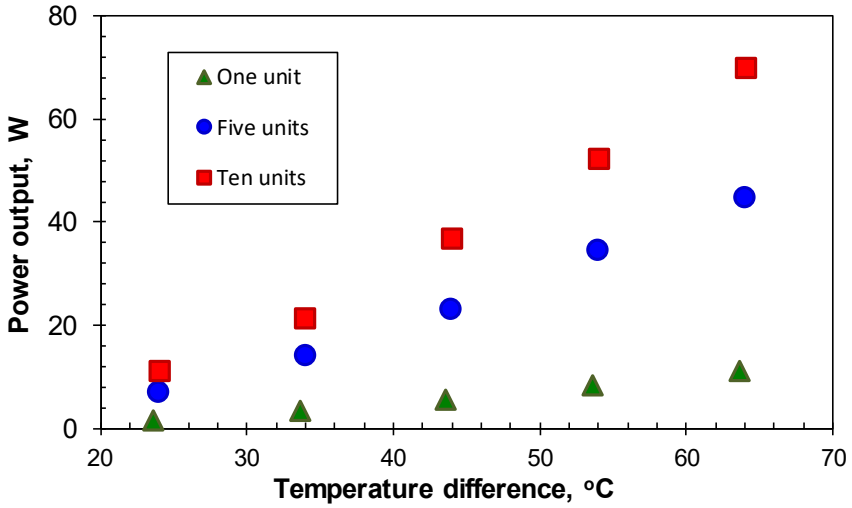

Figure 5: Experimental data of TPF-TEG for three scenarios.

For a thermoelectric power generation system, the framework for holding TEGs and heat exchange always account for a large part of the total cost. Improving the heat transfer efficiency and cutting down the cost simultaneously is always hard to be realized. Figure shows the three different apparatus structures in our previous studies (Chen et al. 2017). The power output of the one-unit TPF-TEG system built in this study was compared with the three different types of framework TEG (Structures a, b and c) in the previous studies (Chen et al. 2017) at the same experimental conditions. The results are shown in Table . One can see that the TPF-TEG device with the structure proposed in this study has a lower water consumption and higher power density. More importantly, the cost of the TPF framework per watt is 3-5 times cheaper than other framework structures. Note that the cost of the framework was calculated based on the real manufacturing cost at the experimental stage. In addition, the proposed TPF structure is more suitable for large-scale production and its cost advantage may be more obvious at the commercial stage.

Table 2: Comparisons among four types of the frameworks (calculations based on experimental data at 63 ºC temperature difference).

Exchanger Type	Fluid Channel Shape	Chip Quantity	Dimensions cm × cm × cm	Ratio of Fluid Channel Volume to Apparent Size	Power Per Chip W	Power Density* W/cm^3	Framework Cost per Watt $/W
Structure a	Holes Type	40	100×10×3	0.08	0.479	0.006	11.85
Structure b	N-Type	40	100×10×5	0.52	0.521	0.004	8.36
Structure c	Rough Surface N-Type	40	100×10×1.8	0.45	0.612	0.014	8.35
TPF Structure	Thin Plate	18	55×13×0.4	0.65	0.622	0.039	2.28

Power Density* is the ratio of power output and apparent volume for one-layer TEG system, W/cm3.

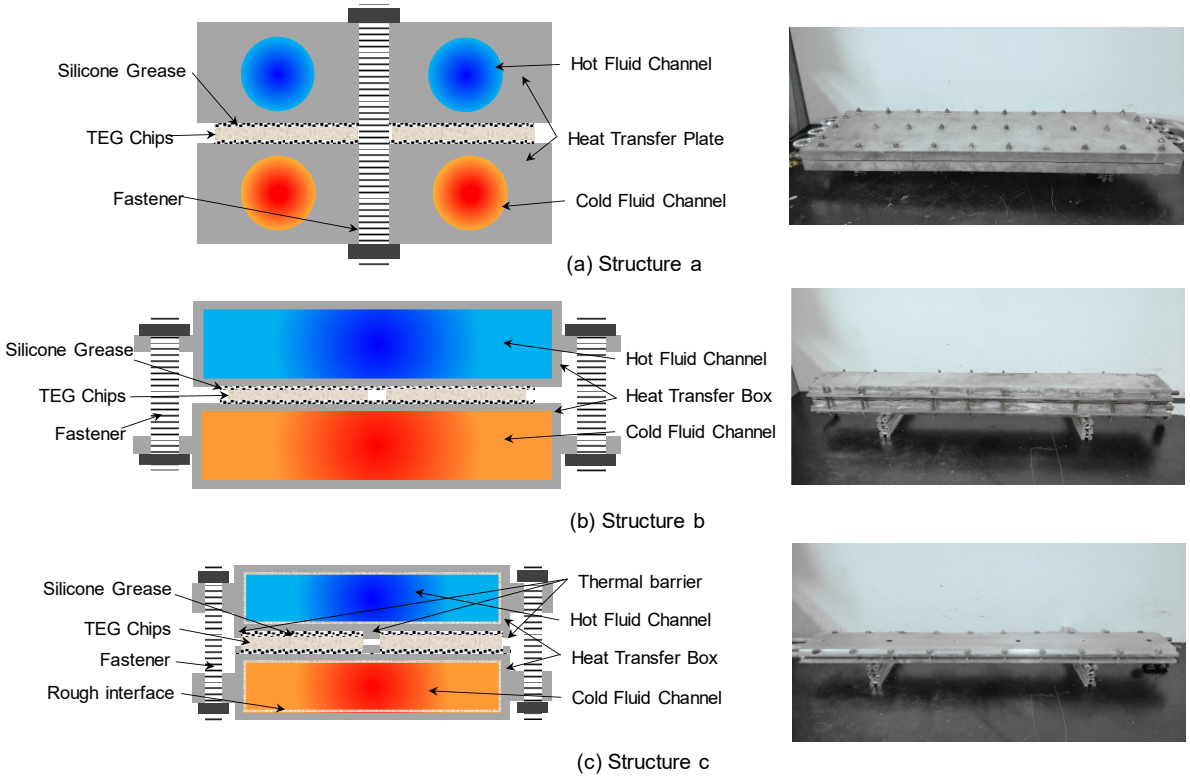

Figure 6: Different TEG apparatus structures in our previous studies: Structures a, b and c (Chen et al. 2017).

4. MODEL DESCRIPTION

The models were established for both TEG chips and TPF-TEG systems respectively. All of the modeling, either for single TEG chip or a TPF-TEG system, was conducted using the finite element software COMSOL Multiphysics.

4.1 TEG Chip Model

The electric current is generated in the TEG chips because of the temperature gradient between two Al_2O_3 ceramics (see Figure 7). All thermoelectric legs in each TEG chip are connected in series by copper conductors (see Figure 3). The TEG chips and the external loads of the circuits are also connected in series. The assumptions made for the electric current model include: 1) all of the TEG chips have identical configurations and properties, and 2) the electrical contact resistance, metallization, and shunt resistances are

negligible. This electric current model utilized the TEG chips of 40 mm×40 mm. Each TEG array contains 18 chips arranged in two rows and nine columns (see Figure 8b).

4.1.1 Governing Equations

A three-dimensional (3-D) model was applied to describe the thermoelectric effect in the TEG chip. The process of heat transfer in solid and the electric current were modeled simultaneously, see **Error! Reference source not found.**.

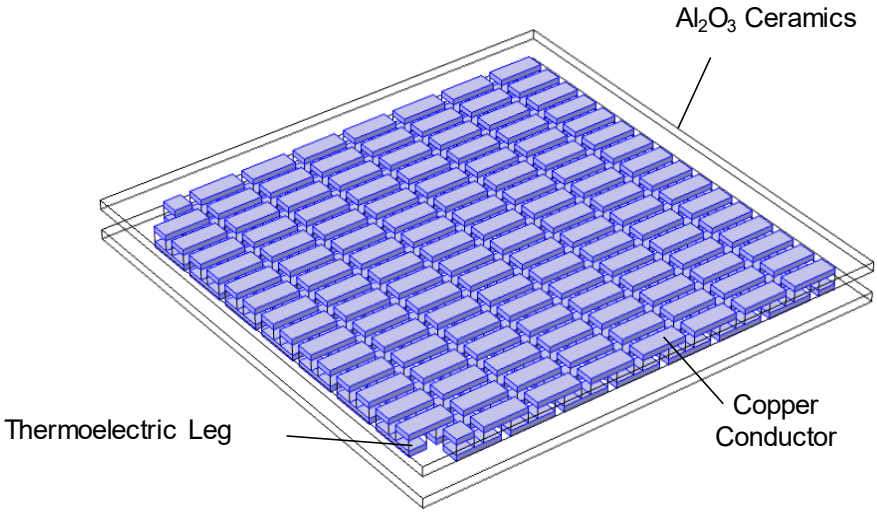

Figure 7: Three-dimensional thermoelectric effect model. Two Al2O3 ceramics are set in the top and bottom; blue color rectangular boxes represent copper conductors; the blocks in-between copper conductors are thermoelectric legs.

The stationary condition is also considered to describe the thermoelectric effect in the thermoelectric legs of the TEG chip. The heat flux describes the heat transfer from one Al_2O_3 ceramic plate to the other Al_2O_3 ceramic plate. In addition to this, there is a heat source generated by the heat effect of the electric current. The equation is expressed as follow:

$$\nabla \cdot \left(-k\nabla T + ST\,\vec{J}\right) = 0 \tag{1}$$

where S is the Seebeck coefficient (V/K), $\vec{J}$ is the electric current density (A/m2) and is given by

$$\vec{J} = \sigma\vec{E} - \sigma S\nabla T \tag{2}$$

where $\vec{E}$ is the electric field intensity (V/m), σ is electrical conductivity (S/m), $S\nabla T$ represents the electromotive force because of the thermoelectric effect. As it can be seen from the above equation, the electric current density is achieved by adding the electric field caused by the thermoelectric effect (the term $-\sigma S\nabla T$). Therefore, thermoelectric effects and heat conduction are coupled in this modeling. The Seebeck coefficient, thermal conductivity and electrical conductivity of copper conductor, P/N-type thermoelectric leg and the Al_2O_3 ceramic are presented in **Error! Reference source not found.**, Figure , A5, and Figure , respectively (see Appendix A).

Table 1: The parameters used in the modelling of the thermoelectric effect.

Copper conductor	Thermal conductivity	400[*W/(m·K)*]
	Electrical conductivity	5.998×10^7 [*S/m*]
Al_2O_3 ceramic	Thermal conductivity	35[*W/(m·K)*]

4.1.2 Boundary Conditions

Heat transfer between thermoelectric legs is not considered. The heat transfer between the thermoelectric legs and air is not considered either. Therefore, the heat fluxes at outer boundaries of the TEG chip are zero, except for the top and bottom boundaries of the ceramic plates. The top and bottom boundaries are in contact with hot- and cold-water channels, respectively. The temperatures at these two boundaries are constant and are given by

$$-\vec{n}\cdot\vec{q}|_{\Gamma_{TC\_outer}} = 0,\ \mathrm{T}|_{\Gamma_{hot}} = \mathrm{T}_{hot}\ ,\ \mathrm{T}|_{\Gamma_{cold}} = \mathrm{T}_{cold} \tag{3}$$

where Γ_{TC_outer} represents the outer boundaries of TEG chip except for the top and bottom boundaries of ceramic plates, Γ_{hot} represents TEG chip's hot side in contact with hot water channel, Γ_{cold} represents TEG chip's cold side in contact with cold water channel, T_{hot} and T_{cold} represent the temperatures of hot- and cold-water channels, respectively.

4.2 TPF-TEG Stack Model

4.2.1 Governing Equations

A 3-D model was applied to describe the whole heat transfer system. Heat exchange takes place between the fluid part (water) and solid part (steel plates and TEG arrays) simultaneously, see Figure .

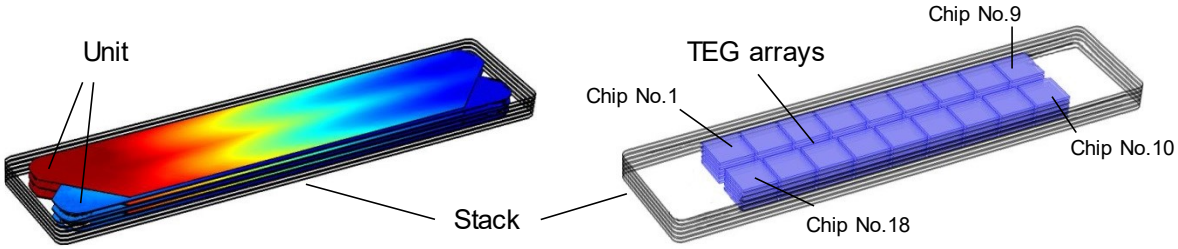

(a) colored parts represent hot- and cold- water channels for TEG chips (b) Inner five arrays of the small box stand

Figure 8: 3-D heat transfer model. The outer transparent region stands for the steel plate.

The stationary governing equation corresponds to the convection-diffusion equation for the steady-state heat transfer process, which contains additional contributions of heat flux (Fourier's law of heat conduction) and no heat source (Bird, Stewart, and Lightfoot 2007). The heat flux describes the heat transfer from the hot water to the steel plate, from the steel plate to the TEG chips, etc. Therefore, the equation is expressed as follow:

$$\rho C_p \vec{u} \cdot \nabla T + \nabla \vec{q} = 0 \tag{4}$$

where ρ is the density (kg/m^3), Cp is the specific heat capacity at constant pressure (J/(kg·K)), T is the absolute temperature (K), $\vec{u}$ is the velocity vector (m/s) and $\vec{q}$ is the heat flux by conduction (W/m2), which can be described by using Fourier's three dimensional diffusion law.

$$\vec{q} = -k\Delta T \tag{5}$$

where k is thermal conductivity (W/(m·K)). The thermal properties of water, TEG chip and the steel plate used in the numerical simulation are presented in Figure -A6 (see Appendix).

4.2.2 Boundary Conditions

As mentioned in the assumptions, all outer boundaries of the TPF-TEG stack are heat-insulated which means the heat fluxes at those boundaries are zero. The temperatures at the inlet of hot and cold water are constant and are given by

$$-\vec{n} \cdot \vec{q}|_{\Gamma_{outer}} = 0, T|_{\Gamma_{hot_{in}}} = T_{hot_w}, \mathrm{T}|_{\Gamma_{cold\_in}} = \mathrm{T}_{cold\_w} \tag{6}$$

where $\vec{n}$ is the normal vector, Γ_{outer} represents the outer boundaries of the TPF-TEG stack, Γ_{hot_in} and Γ_{cold_in} represent the boundaries at inlet of hot and cold water, T_{hot_w} and T_{cold_w} represent the initial temperatures of injected hot and cold water, respectively.

5. MODELING RESULTS

The geometric dimension of the numerical model is identical to that of the experimental apparatus. Figure shows the electric potential of thermoelectric legs when the electric current is 0.3 A, Thot is 68 °C, and T_{cold} is 30 °C. The unit of the color legend is voltage (V). As can be seen from Figure , the electric potential increases when the total number of thermoelectric legs increases. The volt-ampere characteristic curve of a single TEG chip is shown in Figure , the effect of temperature difference on output voltage and electric current is significant. The vertical and horizontal intercept of curves represents the electromotive force and internal resistance of TEG chip at a given temperature difference, respectively.

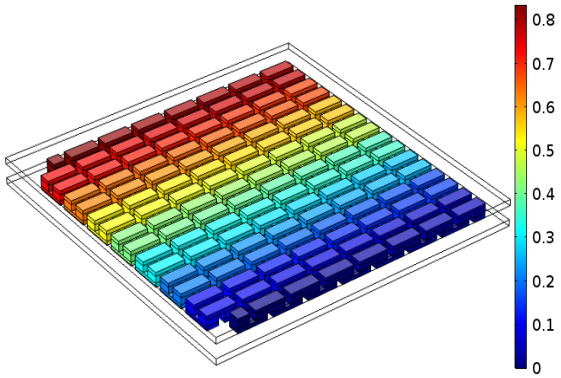

Figure 9: The electric potential distribution of thermoelectric legs.

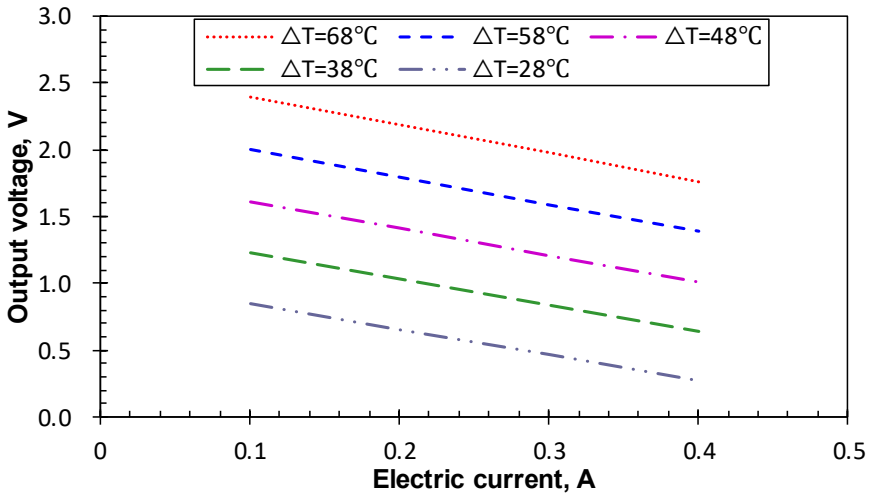

Figure 10: The Volt-ampere characteristic curves for a TEG chip.

The electromotive force and the internal resistance of TEG chip curves are shown in Figure 5, both electromotive force and internal resistance increases with temperature difference, but the change of internal resistance is small.

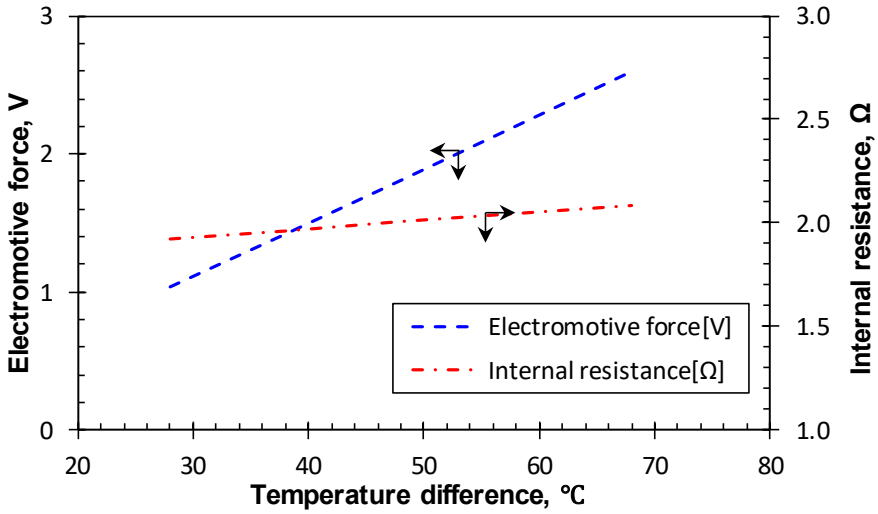

Figure 5: The electromotive force and internal resistance of TEG chip at different temperature differences.

A TPF-TEG stack contains several TPF-TEG units. The number of TPF-TEG units may vary. Figure 6 shows the temperature distribution of a TPF-TEG stack on both cold and hot water sides with five TPF-TEG units. In this case, Thot is 90 ºC, Tcold is 26.1 ºC, and the total hot and cold-water flow rates are 10.71 L/min. The unit of the temperature legend is Celsius degree (ºC). Note that

the temperature legends are labeled for cold and hot water sides respectively for the purpose of clear demonstration. The inlet of cold water is in the lower right corner of the figure. The inlet of hot water is in the upper left corner of the figure. One could optimize the arrangement and the installation of TEG chips according to the temperature distribution on cold and hot water sides. The low-temperature areas (light yellow color) on the top plate in Figure 6 shows the place where has strong heat transfer from hot water to cold water.

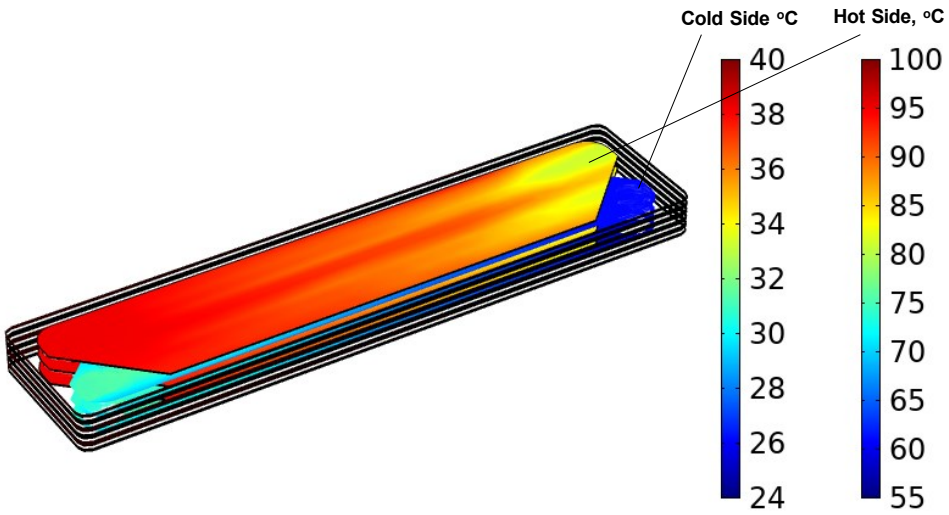

Figure 6: The temperature distribution of TPF-TEG model for five TPF-TEG units.

Modellings of countercurrent and co-current flow between cold and hot water were conducted and the results are shown in Figure 13. The chips are numbered from the chip near the hot water inlet to the outlet, and then from the chip near the cold-water inlet to the outlet (see Figure 8b). The temperature difference is the highest at the chip close to the hot water inlet. It is obvious that the temperature difference of every chip cannot keep at the same value, which leads to a power loss and unstable status. The results indicate that the differences in countercurrent scenarios is smaller than co-current, countercurrent flow can alleviate the problem efficiently.

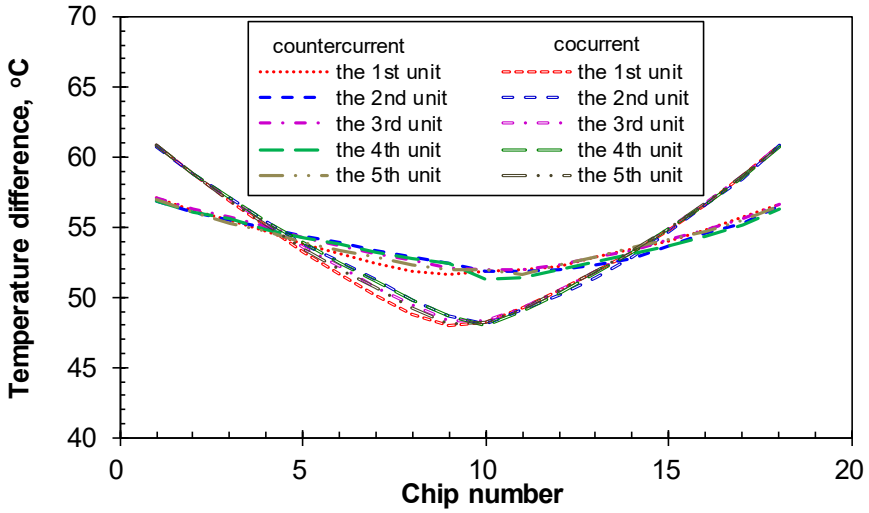

Figure 7: The temperature difference distribution of TEG chips for five units.

In order to compare the modelling and experimental results, the parameters applied in the numerical models are identical to those parameters applied in laboratory experiments. The external load of the current circuit is set equal to the total internal resistance of TEG chips in order to obtain the maximum power output (Yee et al. 2013). It is necessary to input the thermal conductivity values of each part in the numerical TEG models, for example, the ceramic plate, and the bismuth tellurite. However it is difficult to estimate the thermal conductivity values of the contact area between the TEG chips and the ceramic plates. The solution to this problem is described briefly in the following. Firstly we match the experimental data of the temperature differences at the outlet using the model data (see Figures 14a, 15a, and 16a) and obtain the total or equivalent thermal conductivity values of one single TEG chip. Secondly we calculate the power output using the models established in this study with the equivalent thermal conductivity values of TEG chips. Finally we compare the power output data from the modeling with the experimental data (Table). The comparison results are shown in Figures 14-16. One can see that the results simulated by the numerical models match with the TPF-TEG experimental data satisfactorily.

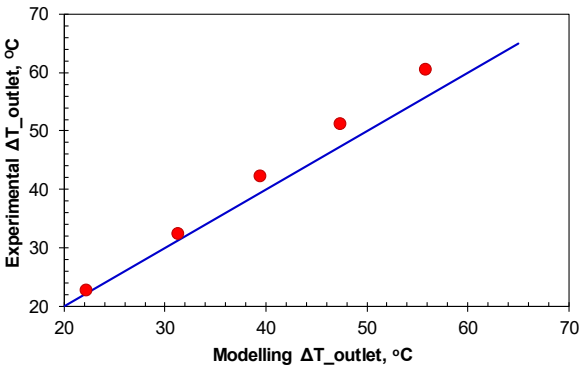

(a) Outlet temperature difference

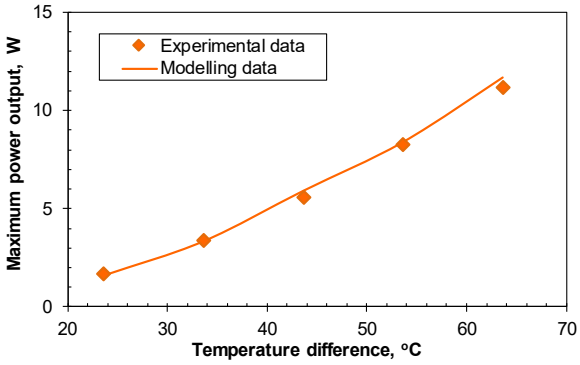

(b) Maximum power output

Figure 8: The fitting results between experimental and numerical data for a single TPF-TEG unit.

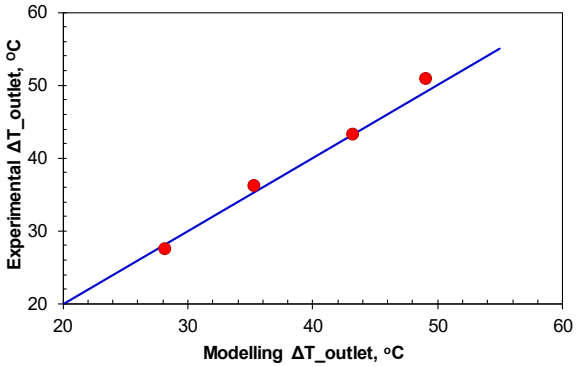

(a) Outlet temperature difference

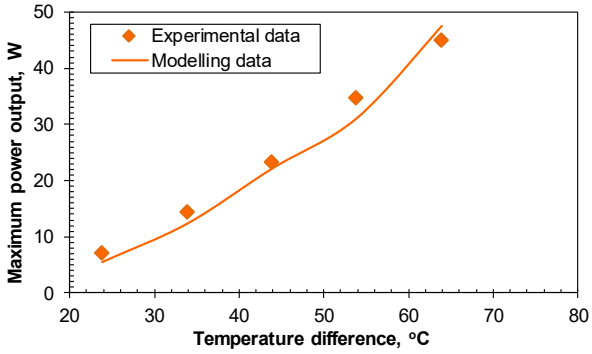

(b) Maximum power output

Figure 9: The fitting results between experimental and numerical data for a five TPF-TEG unit.

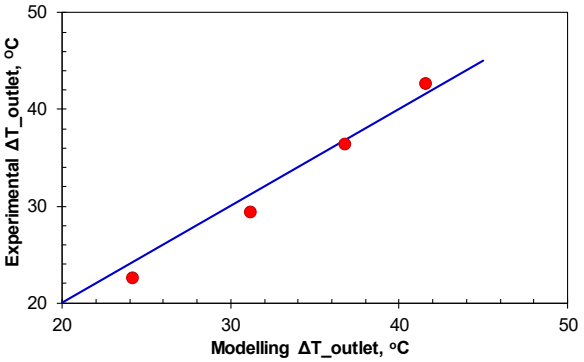

(a) Outlet temperature difference

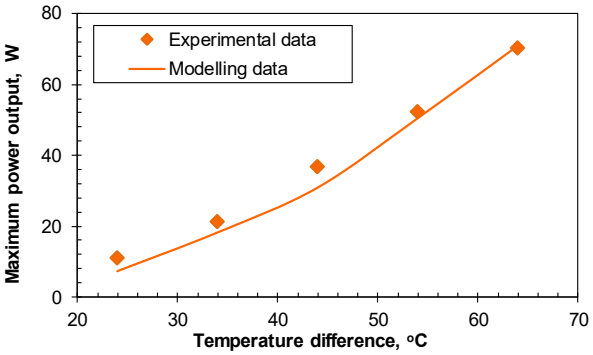

(b) Maximum power output

Figure 10: The fitting results between experimental and numerical data for a ten TPF-TEG unit.

6. CONCLUSIONS

A thermoelectric power generation system with Thin Plate Framework (TPF) has been designed and developed in order to reduce the cost, increase the efficiency and the space utilization ratio. The following conclusions may be drawn based on the experimental and modeling data in this study:

1) The relationship between the power generated by the multi-layer TPF-TEG system and the temperature differences is linear.
2) The power output increase with the water flow rate on hot sides, but not linearly. The optimum flow rate is 8.7 L/min.
3) The specially-designed TPF-TEG has a lower water consumption and higher power density, and its cost per watt is 3-5 times cheaper than other existing models.
4) Numerical TEG models and the corresponding modeling methodology have been established for complex TEG systems with multi-layers of TPF. The modeling results of the power output could match the experimental data of the TEG systems.

ACKNOWLEDGMENTS

This research was conducted partially with financial support from Yangquan Coal Industry (Group) Co., Ltd., the contributions of which are gratefully acknowledged.

REFERENCES

Bamroongkhan, P., C. Lertsatitthanakorn, and S. Soponronnarit. 2019. "Experimental Performance Study of a Solar Parabolic Dish Photovoltaic-Thermoelectric Generator." Energy Procedia 158: 528–33. https://doi.org/10.1016/j.egypro.2019.01.147.

Bird, R Byron, Warren E Stewart, and Edwin N Lightfoot. 2007. Transport Phenomena. John Wiley & Sons.

Chen, Jinlong, Kewen Li, Changwei Liu, Mao Li, Youchang Lv, Lin Jia, and Shanshan Jiang. 2017. "Enhanced Efficiency of Thermoelectric Generator by Optimizing Mechanical and Electrical Structures." Energies 10 (9): 1–15. https://doi.org/10.3390/en10091329.

Demir, Murat Emre, and Ibrahim Dincer. 2017. "Performance Assessment of a Thermoelectric Generator Applied to Exhaust Waste Heat Recovery." Applied Thermal Engineering 120: 694–707. https://doi.org/10.1016/j.applthermaleng.2017.03.052.

Forooghi, Pourya, and Kamel Hooman. 2014. "Experimental Analysis of Heat Transfer of Supercritical Fluids in Plate Heat Exchangers." International Journal of Heat and Mass Transfer 74: 448–59. https://doi.org/10.1016/j.ijheatmasstransfer.2014.03.052.

Goldsmid, H.J., and G.S. Nolas. 2002. "A Review of the New Thermoelectric Materials," 1–6. https://doi.org/10.1109/ict.2001.979602.

Huang, Kuo, Yuying Yan, Bo Li, Yong Li, Kai Li, and Jun Li. 2018. "A Novel Design of Thermoelectric Generator for Automotive Waste Heat Recovery." Automotive Innovation 1 (1): 54–61. https://doi.org/10.1007/s42154-018-0006-z.

Jacobson, Mark Z., and Mark A. Delucchi. 2011. "Providing All Global Energy with Wind, Water, and Solar Power, Part I: Technologies, Energy Resources, Quantities and Areas of Infrastructure, and Materials." Energy Policy 39 (3): 1154–69. https://doi.org/10.1016/j.enpol.2010.11.040.

Jacobson, Mark Z., Mark A. Delucchi, Guillaume Bazouin, Zack A.F. Bauer, Christa C. Heavey, Emma Fisher, Sean B. Morris, Diniana J.Y. Piekutowski, Taylor A. Vencill, and Tim W. Yeskoo. 2015. "100% Clean and Renewable Wind, Water, and Sunlight (WWS) All-Sector Energy Roadmaps for the 50 United States." Energy and Environmental Science 8 (7): 2093–2117. https://doi.org/10.1039/c5ee01283j.

Kim, Hee Seok, Weishu Liu, and Zhifeng Ren. 2017. "The Bridge between the Materials and Devices of Thermoelectric Power Generators." Energy and Environmental Science 10 (1): 69–85. https://doi.org/10.1039/c6ee02488b.

Lee, Heonjoong, Jeff Sharp, David Stokes, Matthew Pearson, and Shashank Priya. 2018. "Modeling and Analysis of the Effect of Thermal Losses on Thermoelectric Generator Performance Using Effective Properties." Applied Energy 211 (December 2017): 987–96. https://doi.org/10.1016/j.apenergy.2017.11.096.

Li, Kewen, Huiyuan Bian, Changwei Liu, Danfeng Zhang, and Yanan Yang. 2015. "Comparison of Geothermal with Solar and Wind Power Generation Systems." Renewable and Sustainable Energy Reviews 42: 1464–74. https://doi.org/10.1016/j.rser.2014.10.049.

Liu, Changwei, Pingyun Chen, and Kewen Li. 2014. "A 1 KW Thermoelectric Generator for Low-Temperature Geothermal Resources." Thirty-Ninth Workshop on Geothermal Reservoir Engineering, no. 2001: 1–12.

Lund, B., and M. D. Zoback. 1999. "Orientation and Magnitude of in Situ Stress to 6.5 Km Depth in the Baltic Shield." International Journal of Rock Mechanics and Mining Sciences 36 (2): 169–90. https://doi.org/10.1016/S0148-9062(98)00183-1.

Lv, Song, Wei He, Qingyang Jiang, Zhongting Hu, Xianghua Liu, Hongbing Chen, and Minghou Liu. 2018. "Study of Different Heat Exchange Technologies Influence on the Performance of Thermoelectric Generators." Energy Conversion and Management 156 (October 2017): 167–77. https://doi.org/10.1016/j.enconman.2017.11.011.

Maneewan, S., and S. Chindaruksa. 2009. "Thermoelectric Power Generation System Using Waste Heat from Biomass Drying." Journal of Electronic Materials 38 (7): 974–80. https://doi.org/10.1007/s11664-009-0820-5.

Saemundsson, K. 2013. "Geology and Gradient Wells." In , 1–9. Lake Bogoria and Lake Naivasha, Kenya, Oct. 29 – Nov. 19, 2010: UNU-GTP, GDC and KenGen. https://orkustofnun.is/gogn/unu-gtp-sc/UNU-GTP-SC-11-14.pdf.

Suter, C., Z. Jovanovic, and A. Steinfeld. 2012. "A 1 KWel Thermoelectric Stack for Geothermal Power Generation-Modeling and Geometrical Optimization." AIP Conference Proceedings 1449: 540–43. https://doi.org/10.1063/1.4731613.

Tan, Gangjian, Li Dong Zhao, and Mercouri G. Kanatzidis. 2016. "Rationally Designing High-Performance Bulk Thermoelectric Materials." Chemical Reviews 116 (19): 12123–49. https://doi.org/10.1021/acs.chemrev.6b00255.

Wang, Tongcai, Weiling Luan, Wei Wang, and Shan Tung Tu. 2014. "Waste Heat Recovery through Plate Heat Exchanger Based Thermoelectric Generator System." Applied Energy 136: 860–65. https://doi.org/10.1016/j.apenergy.2014.07.083.

Yee, Shannon K., Saniya Leblanc, Kenneth E. Goodson, and Chris Dames. 2013. "$ per W Metrics for Thermoelectric Power Generation: Beyond ZT." Energy and Environmental Science 6 (9): 2561–71. https://doi.org/10.1039/c3ee41504j.

Yu, Jianlin, and Hua Zhao. 2007. "A Numerical Model for Thermoelectric Generator with the Parallel-Plate Heat Exchanger." Journal of Power Sources 172 (1): 428–34. https://doi.org/10.1016/j.jpowsour.2007.07.045.

NOMENCLATURE

Cp	specific heat capacity of working fluid, J/(kg·K)
Γ_{hot_in}	boundary of hot water inlet
Γ_{cold_in}	boundary of cold water inlet
Γ_{outer}	outer boundaries of the TPF-TEG module
T_{hot_w}	initial temperature of injected hot water
T_{cold_w}	initial temperature of injected cold water
S	Seebeck coefficient, V/K
$\vec{J}$	electric current density, A/m2
$\vec{E}$	electric field intensity, V/m
σ	electrical conductivity, S/m
Γ_{TC_outer}	outer boundaries of TEG chip except for the top and bottom Al2O3 ceramics
Γ_{hot}	hot side of TEG chip
Γ_{cold}	cold side of TEG chip
T_{hot}	temperatures of hot water channel
T_{cold}	temperatures of cold water channel
ΔThot	temperature difference between the hot water inlet and outlet, K
ΔTcold	temperature difference between the cold water inlet and outlet, K
η	heat-to-electricity efficiency, %
P	electric power output, W
k	thermal conductivity, W/(m·K)
m	mass flow rate, kg/s
$\vec{n}$	normal vector
$\vec{q}$	heat flux by conduction, W/m2
T	absolute temperature, K
$\vec{u}$	velocity vector of working fluid, m/s
ρ	density of working fluid, kg/m3
η	heat-to-electricity efficiency, %

APPENDIX A

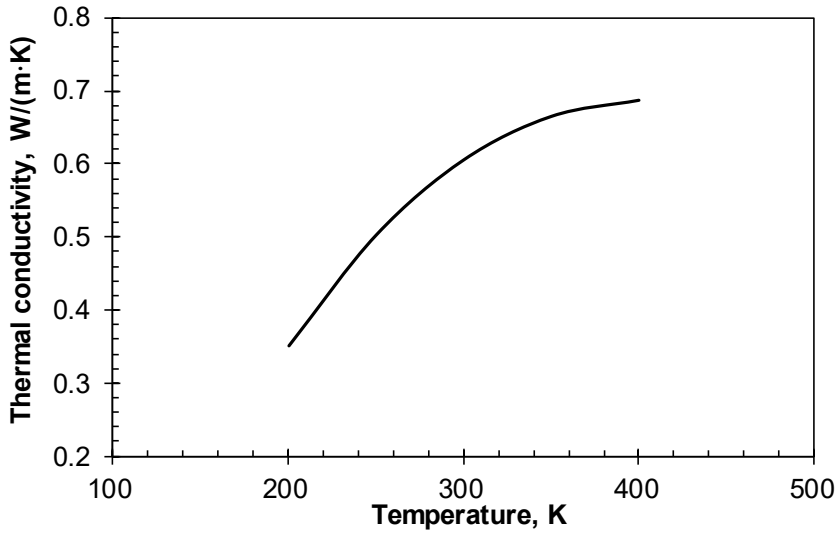

Figure A1: Thermal conductivity curve of water.

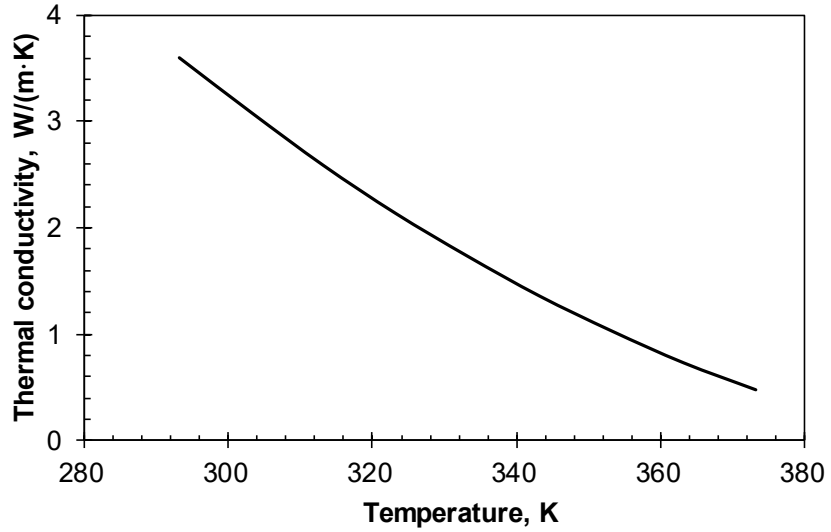

Figure A2: Thermal conductivity curve of TEG chip.

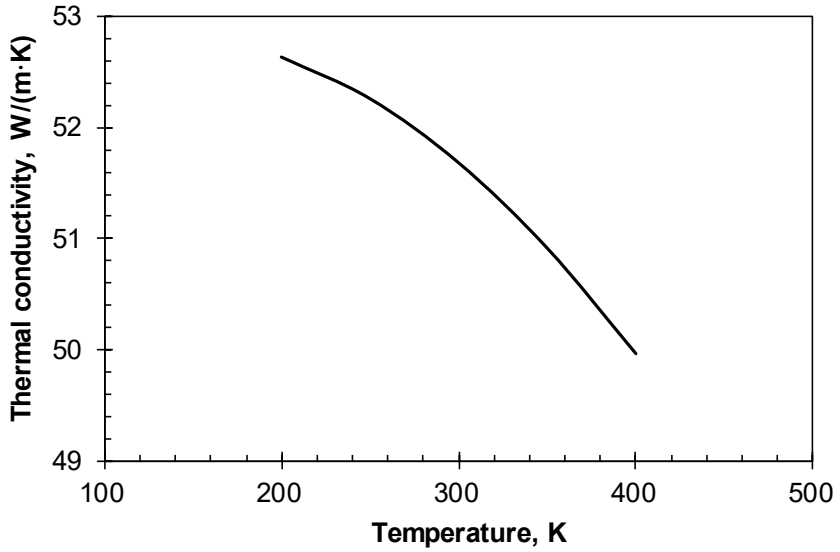

Figure A3: Thermal conductivity curve of steel plate.

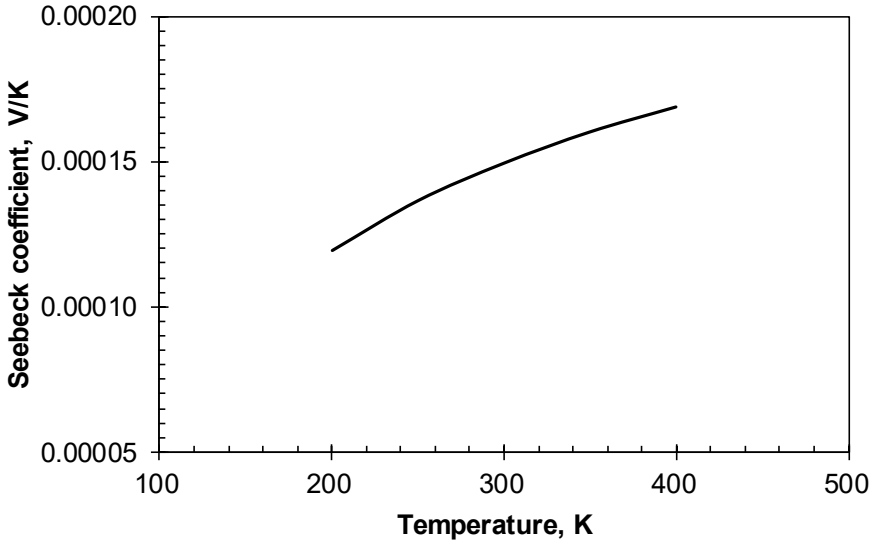

Figure A4: Seebeck coefficient curve of P/N-type leg (in this study, N-type's sign is positive and P-type's sign is negative).

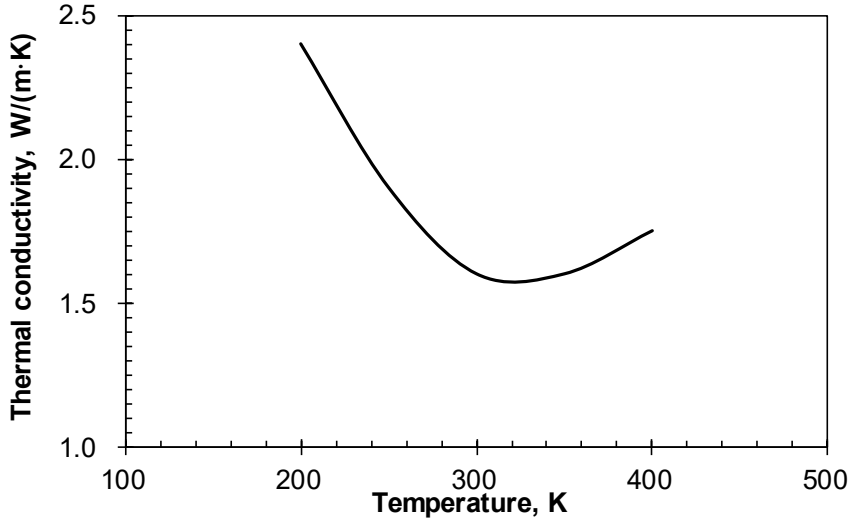

Figure A5: Thermal conductivity curve of P/N-type thermoelectric leg.

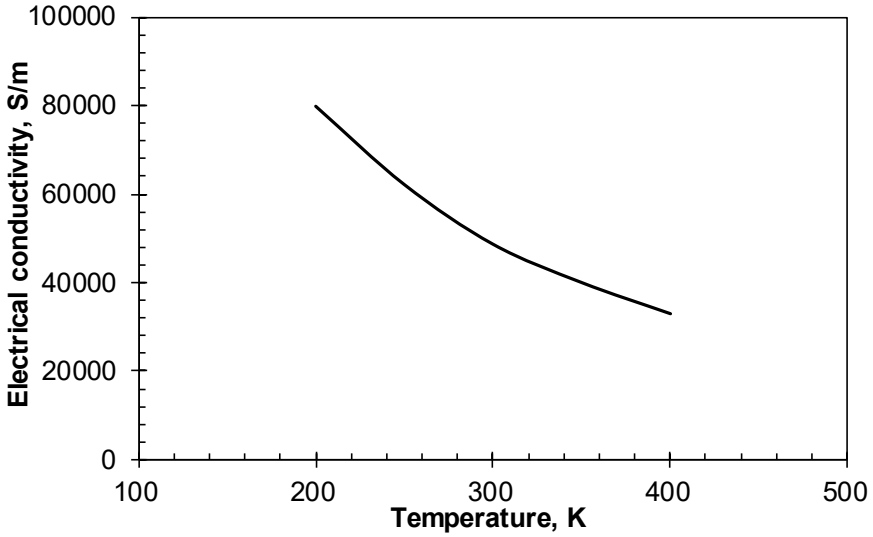

Figure A6: Electrical conductivity curve of P/N-type thermoelectric leg.